Journal of
Materials Chemistry C

PAPER

View Article Online
View Journal | View Issue

Cite this: *J. Mater. Chem. C*, 2015, **3**, 10543

Fast direct synthesis and compaction of phase pure thermoelectric ZnSb†

A. B. Blichfeld and B. B. Iversen*

ZnSb is a promising low cost, non-toxic thermoelectric material, but large scale applications require development of fast and easy synthesis methods. Here a thorough investigation of the influence of synthesis parameters (pressure, sintering time, maximum temperature, stoichiometry) are explored in direct one step Spark Plasma Sintering synthesis of ZnSb pellets from Zn and Sb powders. The homogeneity of the produced pellets is studied using conventional powder X-ray diffraction (PXRD), synchrotron PXRD, and spatially resolved maps of the Seebeck coefficient. Most of the synthesized pellets exhibit a large degree of inhomogeneity caused by zinc migration during the synthesis, but the detailed exploration of the parameter space lead to optimal conditions for producing virtually phase pure pellets. The characterization results from the many samples also suggest that ZnSb is not a line phase as commonly depicted in binary Zn–Sb phase diagrams. Phase pure pellets are used for multi-temperature synchrotron PXRD analysis to study the thermal expansion, thermal stability and lattice dynamics of the system. Based on analysis of atomic displacement parameters obtained from Rietveld refinement of the synchrotron PXRD data, the Debye temperature is estimated to be 175(1) K.

Received 4th June 2015,
Accepted 3rd August 2015

DOI: 10.1039/c5tc01611h

www.rsc.org/MaterialsC

Introduction

Thermoelectric (TE) materials can interconvert heat and electricity, but in order for TE materials to be useful for large scale exploitation of waste heat sources, the materials have to be cheap, abundant, nontoxic, stable in the applied temperature range and have a high thermoelectric efficiency. TE materials are characterized by the dimensionless figure of merit zT:

$$zT = \frac{S^2 \cdot \sigma}{\kappa_E + \kappa_L} \cdot T$$

where T is the absolute temperature, S is the Seebeck coefficient, σ is the electrical conductivity, and κ_E and κ_L are the electrical and lattice contribution to the thermal conductivity, respectively. The electrical properties of TE materials can be quantified by the power factor, $S^2\sigma$ = PF. The conversion efficiency for a thermoelectric generator increases monotonically with zT, and typically a zT value higher than unity is required for the material to be of commercial interest.

The Zn–Sb system is attractive in a thermoelectric context since it consists of cheap and earth abundant elements. During the last couple of decades the β-phase of Zn_4Sb_3 has been the TE material in the Zn–Sb system that has received most attention.[1–6] β-Zn_4Sb_3 has an excellent figure of merit in the intermediate temperature range (100–400 °C), and this is to a large extent due to a highly complex disordered crystal structure, resulting in a very low value of the lattice thermal conductivity.[3] Both at low and high temperature, β-Zn_4Sb_3 undergoes a range of phase transitions to form a variety of polymorphs.[7–9] In addition, recent research has established that the Zn–Sb phase diagram contains a range of unique phases of very similar composition to β-Zn_4Sb_3.[10,11] The huge complexity of the Zn–Sb system around the 4 : 3 composition makes the stability of β-Zn_4Sb_3 problematic, and indeed many studies have addressed the thermal stability of this phase.[12–17] Clearly, a thermally unstable material should not be used in production of a thermoelectric module. Another issue is that the Zn atoms in the structure are highly mobile,[18] and this potentially results in Zn loss from the solid when subjected to strong heat or temperature gradients.[19]

The Zn–Sb binary phase diagram only contains two other well identified phases, namely Zn_3Sb_2 and ZnSb. The latter phase has been known as a TE material since Seebeck discovered the thermoelectric effect.[20] As discussed below ZnSb also has highly attractive TE properties although the maximum zT is lower than for β-Zn_4Sb_3.[21] For this reason much less research has been devoted to ZnSb, and often ZnSb has merely been considered as an impurity phase in Zn_4Sb_3-type materials.[22] The structure of ZnSb is much simpler than any of the polymorphs of Zn_4Sb_3, and therefore the thermal conductivity of ZnSb is expected to be considerable higher than for Zn_4Sb_3.[23] This has been confirmed experimentally with ZnSb and Zn_4Sb_3 having thermal

---

Centre for Materials Crystallography, Department of Chemistry and iNANO, Aarhus University, Langelandsgade 140, DK-8000 Aarhus C, Denmark. E-mail: bo@chem.au.dk

† Electronic supplementary information (ESI) available. See DOI: 10.1039/c5tc01611h

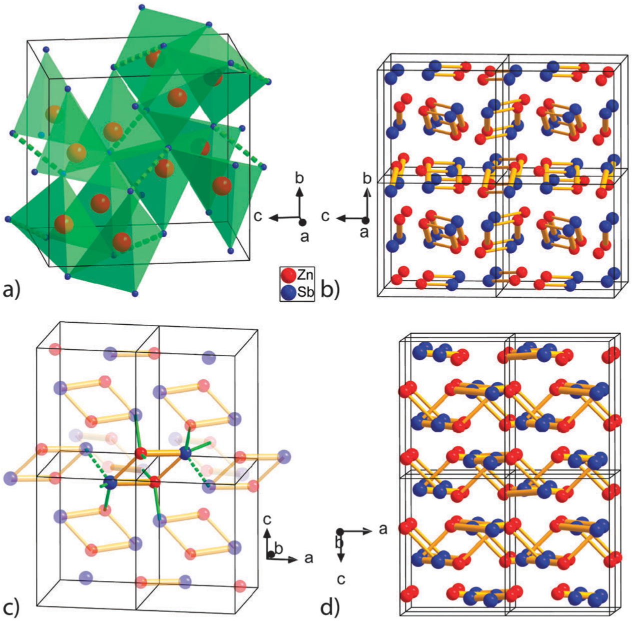

Fig. 1 The crystal structure of ZnSb represented in different directions highlighting structural units. The thin and thick yellow bond shows the short and long Zn–Sb bonds, respectively. (a) Shows the distorted tetragonal coordination of Zn, (b) eight unit cells along the *a*-axis, (c) the coordination of the Zn–Sb diamond, and (d) eight unit cells along the *b*-axis. The solid green bond are the so called 2c2e bonds, and the dashed green bond are the Sb–Sb dumbbell.

conductivities of ∼2 and below 1 W m^{-1} K^{-1}, respectively.[3,24] The structure of ZnSb can be derived from the normal III–V or II–VI semiconductors, which have a cubic diamond structure with tetrahedral coordination. The unit cell of ZnSb is primitive orthorhombic ($Z = 8$), where the tetrahedra are distorted, allowing for edge sharing besides corner sharing, see Fig. 1a.[25]

Even though ZnSb is a relatively simple structure, the chemical bonding and electron counting in the structure is rather complex. ZnSb can be considered as a II–V semiconductor, and an ionic approach would then suggest the presence of Zn^{2+} and Sb^{2-} ions in the Zintl phase; eight positive Zn^{2+} cations in the unit cell donate electrons to four anionic ${Sb_2}^{4-}$ dimers, indicated by the dashed green bond in Fig. 1a. The covalent approach can be rationalized upon careful considerations of the structure if Zn and Sb form Zn_2Sb_2 diamond shaped units with a 4 center 4 electron (4c4e) covalent bond, see Fig. 1c.[25] The diamond is asymmetric and has two short and two long Zn–Sb bonds (Fig. 1). In addition each Zn_2Sb_2 unit has ten normal 2 center 2 electron (2c2e) covalent bonds (Fig. 1c) to other units giving an electron count per 4 atoms of 10 + 4 = 14, which equals 3.5 per atom. The diamond shaped Zn_2Sb_2 motif has also been used to rationalize structures of the Zn_4Sb_3 phases.[26] The main problem with the ionic view of the ZnSb structure is that it is contradicted by elaborate electron density analysis, which shows that both Zn and Sb are close to neutral, and the structure is probably best understood as a covalent network structure.[27] In Fig. 1b and d, eight unit cells are shown along the *a*- and *b*-axis, respectively. Fig. 1b highlights the rows of the Zn_2Sb_2 diamonds along the *a*-axis with 2c2e bond between and in Fig. 1d the rows are viewed from the side where Sb dumbbells connect the diamonds along the row. Because of the simple well-ordered structure of ZnSb compared with β-Zn_4Sb_3, many theoretical studies include ZnSb as a reference, and indeed theoretical analysis is much better established for ZnSb.[27–31] The band gap is larger in ZnSb in comparison to β-Zn_4Sb_3, and the Seebeck coefficient is between 2–3 times greater for ZnSb.[3] The larger band gap results in a smaller amounts of charge carriers, and therefore a reduced electrical conductivity, but because of the second power on the Seebeck coefficient, as a result the PF is 1–3 times larger for ZnSb than for Zn_4Sb_3 depending on the charge carrier concentration. For optimized β-Zn_4Sb_3, with $n = 7.5 \times 10^{19}$ cm^{-3} the PF $\approx 8 \times 10^{-4}$ W m^{-1} K^{-2},[3] and along the *c*-axis in a single crystal ZnSb up to 3 times larger.[21] The excellent power factor in ZnSb has meant that much research has aimed at lowering the thermal conductivity.

One way of lowering the thermal conductivity is to reduce the particle size. Mechanical grinding (MG) was used as a post synthesis treatment with ZnSb prepared by melt synthesis and subsequent hot-pressing, and revealed a $zT = 0.8$ at 550 K.[32] The high zT stems from a reduction of the thermal conductivity to ∼1/3 compared with the single crystal values.[21] Thermal conductivities even lower than 1 W (K $m)^{-1}$ has been reported recently where cryo-milling of ZnSb prepared by melt synthesis and subsequent SPS compaction was employed.[33] An alternative approach is to have nano-inclusions of another phase inside the ZnSb matrix.[34] This was done in a study by Valset *et al.*, where Zn_3P_2 nanoparticles were added in various amounts to ZnSb, and with 2.5 at% Zn_3P_2 and 0.2 at% Cu a zT value of 0.9 was reached at 550 K.[35] The presence of phosphor increased the solubility of the Cu dopant in the solid solution, which had the combined effect of lowering the thermal conductivity and increasing the PF to give a high zT. The same effect was seen in ZnSb with 0.15 at%, Ag, 3 at% Cd, and 3 at% Sn, resulting in $zT = 1$ at 630 K.[36] The highest zT reported for ZnSb was reported by Xiong *et al.* where Ag doping ($x = 0.002$) in $Zn_{1-x}Ag_xSb$ gave $zT = 1.15$ at 570 K.[24] Ag was proposed to act both as a dual function as dopant and as Ag_3Sb nanoinclusion. A third way of reducing the thermal conductivity is by reducing the dimensionality of the material,[37] which can be done by production of thin-films. Thermal conductivities are challenging to measure for thin-films due to the presence of the substrate, which is $\sim 10^3$ times thicker than the film. Sun *et al.* reported DC magnetron sputtering of phase pure ZnSb thin films,[11] and the TE properties of ZnSb thin films were therefore evaluated *via* the PF, and a value of 16.5×10^{-4} W m^{-1} K^{-2} at 573 K was achieved. This is to be compared with a value of 12×10^{-4} W m^{-1} K^{-2} at 553 K for phase pure β-Zn_4Sb_3 thin films. Since the thermal conductivity was unavailable, the value of the bulk materials was used to make a (very) conservative estimate of $zT \approx 0.6$ at 573 K for ZnSb thin films. In the attempt to make phase pure β-Zn_4Sb_3, Wrona *et al.* obtained ZnSb as a byproduct.[38] Grinding elemental powders in nominal composition Zn : Sb = 4.14 : 3 then subsequent Spark Plasma Sintering (SPS) synthesis at 673 K for 1 hour, they obtained the ZnSb phase. 1 mm at each side of the pellets was abraded before PXRD data were recorded and it is unclear what part of the sample was used.

As mentioned above application of new TE materials is only possible if fast synthesis methods capable of producing substantial amounts of material can be developed. Recently, we reported on direct synthesis and compaction of phase pure β-Zn_4Sb_3 by SPS.[39] In this work we present a comprehensive exploration of the synthesis parameter space in order to establish if it is possible to synthesize phase pure ZnSb by SPS. Besides being of significant interest as a method for producing TE materials, the present synthesis method is also of significant general interest for precisely controlling the stoichiometry of pressed pellets that can be used as targets in DC magnetron sputtering of Zn–Sb thin films. First the synthesis procedures towards phase pure ZnSb will be described. Subsequently, the crystal structure and thermal stability will be examined in detail through elaborate multi-temperature synchrotron X-ray powder diffraction measurements.

Experimental

Zinc powder (99.99%, grain size < 45 μm, MERCK KGaA) and antimony powder (99.5%, grain size < 150 μm, SIGMA-ALDRICH CHEMIE GmbH) were weighed in a molar ratio of 1 : 1. The powders were mixed in a ball mill mixer (SpectroMill, CHEMPLEX INDUSTRIES, INC) for 15 min. 13 g of the mixed powder was then loaded into a 25.4 mm diameter high density graphite die protected by BN spray, and SPS pressing was carried out using an SPS-515 instrument (SPS SYNTEX INC, Japan). The direction of the pulsed direct current is from the lower piston to the upper piston in the instrument employed. The densities of the as-pressed discs were measured using the Archimedes technique. Powder X-ray diffraction measurements (PXRD) were carried out on both sides of a gently polished pellet using a Rigaku Smartlab equipped with a Cu K_α source and parallel beam optics. The pellet was then cut through the center of the cylinder along the axis the pressure was applied, resulting in two half cylinders. Seebeck microprobe scanning was performed on the cross section of one of the pellets using a PANCO PSM.[40] During the PSM measurement, the sample surface is touched by a heated tungsten tip, which moves between measurements. This results in a spatially resolved map of the Seebeck coefficient with a resolution of ~50 μm.[40] After polishing the surface of the cross section, the pellet was sandwiched between two Ni pieces to ensure the whole width of the pellet was available to the PSM tip. Scanning Electron Microscopy (SEM) and Energy Dispersive X-Ray spectroscopy (EDX) data were measured using a FEI NOVA 600 Nano SEM equipped with a TLD detector in secondary electron mode, and all images were taken under high vacuum. For selected samples synchrotron PXRD data were measured on beamline BL44B2 at the SPring-8 synchrotron facility in Japan using powder from the main body of the pellets. The synchrotron wavelengths were obtained from Rietveld refinement of data measured on a CeO_2 standard, and they were λ = 0.500529(2) Å and λ = 0.500451(2) Å for the low temperature (LT) and high temperature (HT) measurements, respectively. The data were collected from $2\theta = 2.5°$ to 77° covering 15.6 $Å^{-1}$. The powder samples were prepared by using a powder floating technique in ethanol for size selection, and the powder was packed in 0.1 mm glass and quartz capillaries for LT and HT measurements, respectively. In the multi temperature data collection a heating ramp of 100 K min^{-1} was used with an equilibration time of 60 seconds. The acquisition time was 5 min for each data set. Rietveld refinements were performed using the FullProf program.[41] User defined anomalous scattering factors were used for the synchrotron refinements; Zn: f' = 0.2435, f'' = 0.7644, Sb: f' = −1.6081, f'' = 0.8245, and O: f' = 0, f'' = 0.002. The initial starting models for Rietveld refinement were generated from ICSD codes for ZnSb(55403), Sb(64695), ZnO(26170), and $ZnSb_2O_4$(31996).

Results and discussion

A number of experimental parameters were investigated to determine their influence on the direct synthesis of ZnSb *via* SPS; pressure (P), sintering time (t_{sint}) and maximum temperature (T_{max}). The influence of excess Zn or Sb was also studied.

All pellets had a relative density (δ) between 97% and 101% compared to the theoretical density of ZnSb (6.377 g cm^{-3}). The theoretical densities of Zn_4Sb_3, Zn and Sb are 6.361 g cm^{-3}, 7.146 g cm^{-3}, and 6.707 g cm^{-3}, respectively. If a pellet is a mixture of ZnSb and Zn_4Sb_3, then the density is not likely to be affected, perhaps lowered. If unreacted Zn or Sb are present, this will influence the density to a larger extent. Thus, the range of the relative densities determined in this work suggest that none of the pellets contain significant quantities of unreacted Zn or Sb. The influence of the different SPS parameters will be discussed below in individual paragraphs.

All pellets have been analyzed by PSM where the current has propagated left to right. The Seebeck coefficient is mapped for each scan together with a histogram of the Seebeck values fitted with a Gaussian function (red curve). In addition a cumulative count of points for the map (blue curve) is given, and this count reaches 100% at the maximum of the Gaussian curve. For all the PSM scans the ''blue'' sections on both sides correspond to the Ni-pellets (S = −12 μV K^{-1}) sandwiching the sample. The same color scale for the Seebeck coefficient has been used for all scans (0–300 μV K^{-1}), and this scale covers the whole range of Seebeck coefficients in the cumulative curves. An overview of all the produced samples is given in the ESI† Fig. S1.

Visual inspection of the Seebeck map provides an indication of the homogeneity of a given sample. Distinct colors refer to unique phases, which can be either different electronic phases (different doping level) or phases with different crystal structures and compositions. For phase pure Zn_4Sb_3 prepared in one step synthesis *via* SPS, the Seebeck coefficient measured with the same PSM system is S = 90 μV K^{-1},[39] and this corresponds to a light blue color on the scale used in the present work. The range of Seebeck coefficients for Zn_4Sb_3 made by other methods typically varies from 90–130 μV K^{-1} in PSM scans.[13] In the study by Dasgupta *et al.* ZnSb was identified with a Seebeck coefficient of 150 μV K^{-1} and above.

Applied pressure

The effect on the homogeneity and phases for different applied pressures were examined for pellets made at 723 K, a ramping time of 10 minutes, sintering times of 10 and 15 minutes, and pressures of 50 and 100 MPa. The PSM scans can be seen in Fig. 2.

There are no significant discrepancies in the PSM data between preparations at low and high pressure. One should note, however, that at higher pressures there is a small reduction in the distinct green/yellow phase, where $S = 175$ μV K^{-1}. For the two pellets pressed at 100 MPa, layers along the faces are observed with a green (~150 μV K^{-1}) layer at the left and a light blue (~100 μV K^{-1}) at the right for the 10 and 5 minutes pellets, respectively. An increase in Zn at the right hand side and a decrease of Zn at the left hand side may be due to Zn-ion migration, as previously seen in Zn_4Sb_3.[19] As also confirmed by PXRD in Fig. 3, the light blue phase on the right side is Zn_4Sb_3, which has a larger Zn content than the overall stoichiometry of the sample. The Zn migration seems to occur faster at higher pressures, which will contribute to a faster phase segregation and thus aid in the search of the conditions required for a phase pure sample. The density of the two samples synthesized at 50 MPa are the lowest of all samples in this study. This further indicates that Zn migrates faster or easier at higher pressures resulting in a larger physical movement of Zn ions between grains, leading to higher densities. Therefore a pressure of 100 MPa was used for the following pellets.

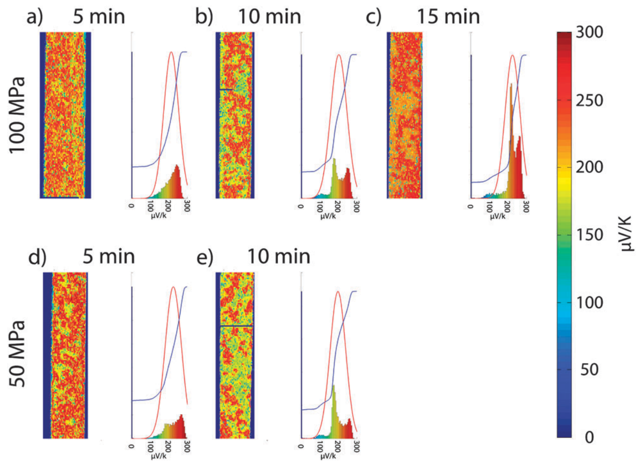

Fig. 2 PSM scans of pellets made at 673 K, a ramping time of 10 minutes, was used various reaction times, alternative applied pressure of 50 MPa and 100 MPa for the bottom and top row respectively, and varying sintering times indicated at the top of the individual scans. The current enters the pellet from the left side. The blue regions on each side of the scans are Ni-pellets enabling a scan of the full height of the pellet. All maps and histograms use the same μV K^{-1} scale, given on the right side. Blue lines in the data of the pellet are the result of errors in the data acquisition of those points.

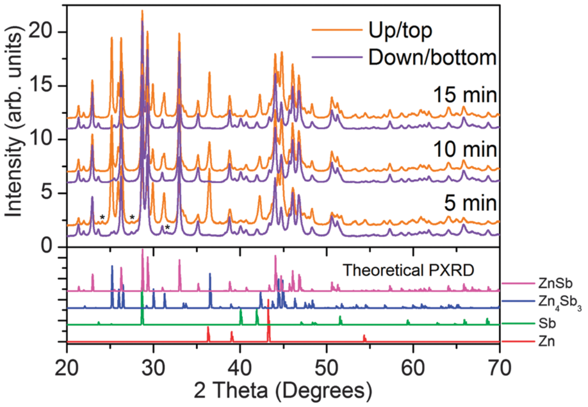

Fig. 3 PXRD patterns (20° < 2θ < 70° Cu-K_α) of the top and bottom sides of pellets made at 100 MPa pressure, 673 K and different sintering times. In all the patterns from the bottom sides about 5 wt% elemental Sb is still present as determined by Rietveld refinement (Table S1, ESI†) of the data for the 5 min pellet. Unknown impurity peaks are marked by an asterisk.

Sintering time

The influence of the reaction time was investigated for different maximum temperatures using a ramping time of 10 minutes and a pressure of 100 MPa (see the ESI† for an overview, Fig. S1). Focusing on Fig. 2a–c the effect of the sintering time is illustrated clearly. A reaction time of 5 minutes (Fig. 2a) results in a broad distribution of the Seebeck coefficient, and indicates that the reaction is incomplete; a mixture of β-Zn_4Sb_3 and ZnSb is obtained rather than a single phase. From the Seebeck map it is seen that there is little evidence to suggest segregation, except at the top and bottom as seen by the layers along the surfaces. For the sample sintered for 10 minutes (Fig. 2b) two distinct peaks are observed in the distribution (a green and a red phase) with Seebeck coefficients of 165 μV K^{-1} and 255 μV K^{-1}, respectively. In the Seebeck map it is clear that these two phases segregate into distinct regions in the pellet. For the pellet sintered for 15 minutes (Fig. 2c), two peaks are also observed, but the lower peak has shifted to a higher Seebeck coefficient of 215 μV K^{-1} corresponding to an orange phase. The relative intensity of the orange phase in Fig. 2c has increased compared with the red phase in Fig. 2b. This suggests that an increased sintering time increases the overall Seebeck coefficient of the pellets, but also results in distinct phase segregation. From the PXRD patterns in Fig. 3, it is clear that the two outer faces of the pressed pellets are not identical. Rietveld refinements on the PXRD data for the pellets indicate that the top sides contain a mixture of ZnSb and Zn_4Sb_3, and for the pellet sintered for 5 minute the ratio is approximately 38 *vs.* 60 wt%, respectively (Table S1, ESI†). In addition ~2 wt% elemental Sb and ~1 wt% Zn is still present in the 5 minute sample at the top. The current enters the pellet from the bottom and migration of Zn-ions results in excess Zn at the top (right side in PSM scans). This excess leads to the formation of Zn_4Sb_3, as was also observed in the work of Yin *et al.*[39] In all PXRD patterns measured from the bottom sides of the pellets, about 5 wt% elemental Sb is present, but no Zn_4Sb_3 is observed (Table S1, ESI†). In the 5 minute pellets reflections from small amounts of impurity phase were also observed, but these are absent from data for samples prepared for longer sintering times. The impurity peaks do not match any of the known oxides of Zn and Sb, BN phase or combinations of Zn_xSb_y. Interestingly, there is no difference in the phase compositions obtained from PXRD Rietveld refinement (Table S1, ESI†) on the bottom side of the pellets pressed for 10 and 15 minutes, even though clear differences are observed in the corresponding Seebeck maps (green and orange phases, respectively).

Maximum temperature

The effect of changing the maximum sintering temperature was investigated for pellets made with at 100 MPa, a ramping time of 10 minutes and sintering times of 5, 10, and 15 minutes (see ESI,† Fig. S1). The largest differences are seen in the 10 minute series, see Fig. 4, and these will be discussed here. At the lowest temperature of 573 K, the peak in the Seebeck histogram is around 75 μV K^{-1} (light blue region). This value is even lower than the Seebeck coefficient of Zn_4Sb_3, which is around 90 μV K^{-1} (for pellets pressed with an additional Zn foil).[39] Since the Seebeck coefficient for metals is very low, this could indicate that the mixed powders have not fully reacted. In the PXRD in Fig. 5, peaks corresponding to elemental Sb are visible in addition to the ZnSb and Zn_4Sb_3 phases. An EDX map was collected on the same surface, and large regions with high Sb concentrations and low Zn concentrations were seen (Fig. S2, ESI†). Synchrotron PXRD measurements were carried out on material extracted from the main body of the pellet made at 573 K, and Rietveld analysis gives a phase composition of 67.8(2) wt% ZnSb, 8.47(6) wt% Sb, and 23.7(2) wt% Zn_4Sb_3 (Table S2, ESI†). No elemental Zn was observed in the synchrotron PXRD data (Fig. S3, ESI†). Since a reaction between Zn and Sb takes place even at the lowest temperature, which is far below the melting point of the elements and the Zn–Sb compounds, it is believed that the current passing through the sample, resulting in Zn migration, does play an important role for the direct synthesis.

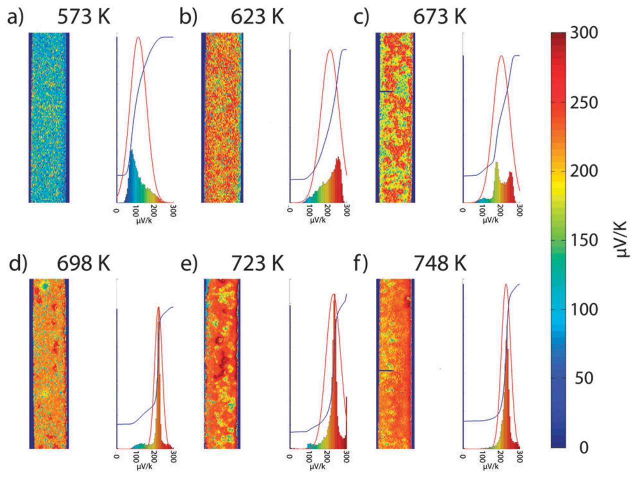

Fig. 4 PSM scans of pellets prepared at different temperatures, 100 MPa pressure, a ramping time of 10 minutes and sintering time of 10 minutes.

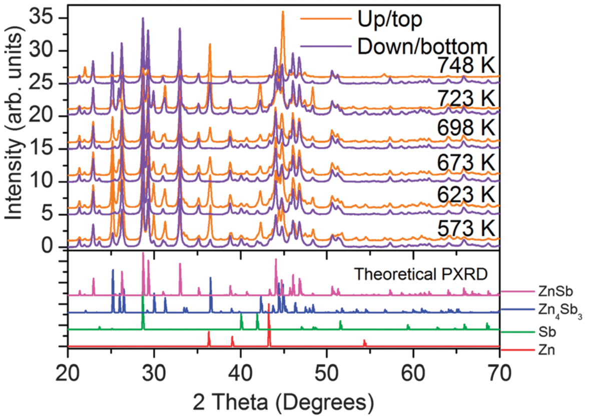

Fig. 5 XRD patterns (20° < 2θ < 70° Cu-K$_\alpha$) on the top and bottom sides of pellets made at different temperatures, an applied pressure of 100 MPa, a ramping time of 10 minutes and reaction time of 10 minutes.

The distribution of Seebeck coefficients (Fig. 4b) is much broader than expected from the PXRD phase composition analysis. This suggests that a smooth change in the electrical properties of ZnSb is possible without abrupt structural changes. In other words ZnSb may not be a line phase as indicated in most phase diagrams, opening up for formation of Zn vacancies to a large degree. In fact this has been seen in a high temperature study of Zn_4Sb_3, where $Zn_{1-x}Sb$ was observed as a reaction product after heating under vacuum.[42] Theoretical studies have shown that Zn-vacancies are the origin of the p-type conductivity observed in ZnSb, but the expected concentration of such defects was so small that it was not considered a deviation from a line phase of ZnSb.[43]

At 623 K the peak of the wide distribution shifts to 255 μV K^{-1} (red region). This shift indicates a higher rate of conversion to the ZnSb phase, but elemental Sb is still observed in the PXRD data, Fig. 5. From Rietveld analysis (Table S1, ESI†), the bottom side has no contribution from Zn_4Sb_3, but the top side contains 49 wt% Zn_4Sb_3 48 wt% ZnSb and 2 wt% Sb. It is clear from the PSM scan that the top side contains a layer of the blue phase, and this is consistent with migration of Zn ions in the direction of the current flow. At the two lowest temperatures of 573 K and 623 K, the Seebeck distributions are very broad. However, when the temperature is increased to 673 K, two distinct phases start emerging; a green/yellow phase with a Seebeck coefficient of 175 μV K^{-1}, and the red phase with Seebeck coefficient of 255 μV K^{-1}. The red and green regions are distributed throughout the entire pellet, and it almost looks like the result of quenching an ongoing reaction. The PXRD data from the bottom side, does not indicate the presence of Zn_4Sb_3, whereas the topside still contains Zn_4Sb_3 (but no Sb). The Zn_4Sb_3 region observed in the Seebeck map is not as thick as seen for the two lower temperatures. Since the ZnSb phase is the most thermodynamically stable phase, going to higher temperatures could assist in decreasing the formation of Zn_4Sb_3 at the topside.

Increasing the temperature to 698 K has a drastic effect on the phases present in the Seebeck map. The yellow/green phase and the red phase almost completely disappear, and an orange phase with $S = 215\ \mu V\ K^{-1}$ dominates. This phase was also seen in Fig. 2c, but mixed with the red phase. Blue/green spots are homogeneously distributed within the main body of the pellet. The PXRD pattern for the top side of the pellet pressed at 698 K shows the least Zn_4Sb_3 among the samples in the temperature series, Fig. 5. Rietveld refinement gives a phase composition of 28 wt% Zn_4Sb_3 and 72 wt% ZnSb (Table S1, ESI†), in addition to a trace of the same unidentified impurity phase also observed in Fig. 3.

When the temperature is increased to 723 K, the Seebeck coefficient of the main body of the pellet shifts to $235\ \mu V\ K^{-1}$ indicated by a dark orange color. In this pellet, the blue/green spots disappear and a dark red phase appears (Fig. 4e). This is the only PSM scan that exceeds the chosen color range, but from $300\ \mu V\ K^{-1}$ the histogram decreases linearly to zero at $330\ \mu V\ K^{-1}$. The PXRD data show Zn_4Sb_3 on both sides of the pellet; which corresponds to the light blue regions in the Seebeck map. This is the only sample where this happens and the origin is unclear. At 748 K, the dark orange phase dominates in the pellet. The PXRD data show that the bottom side is pure ZnSb, whereas the top side consists of ZnSb and highly oriented Zn_4Sb_3 which gives rise to very intense peaks that are not refinable. In Fig. 6e an average of the measured Seebeck coefficient along the x- and y-direction of the PSM scan is shown. It is clear that there is a gradient in the Seebeck coefficient along the x-direction. This is the same direction as the pressure and current gradient and the higher Seebeck value is observed at the top where the current exits. A thin layer of β-Zn_4Sb_3 with lower Seebeck value is seen at the very surface, and this is confirmed by the PXRD data. Immediately prior the top there is a rise in the Seebeck value, and this could be Zn deficient $Zn_{1-x}Sb$, where the missing Zn has migrated to the surface. Synchrotron PXRD was performed on the powder extracted from the main body of the pellet, and Rietveld refinement confirmed the purity of this sample with ZnSb wt% 99.1(2) and 0.89(5) wt% Sb (Table S2, ESI†).

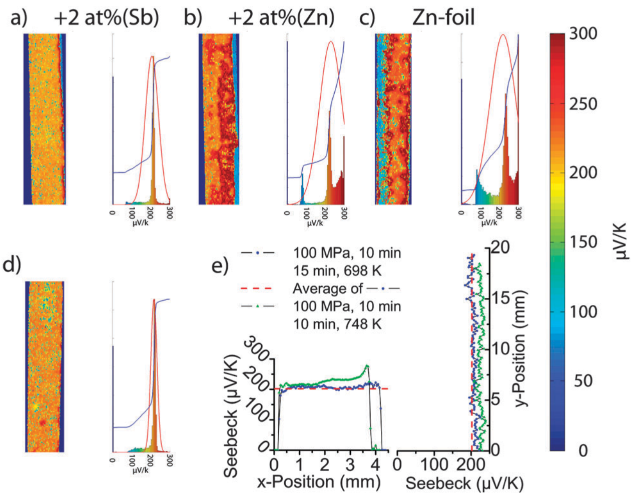

Fig. 6 (a)–(c) PSM scans of pellets at 100 MPa, ramping time of 10 minutes, a sintering time of 15 minutes, and a maximum temperature of 723 K. In (a) 2 at% extra Sb was added, (b) 2 at% extra Zn was added, and in (c) a Zn-foil was added to the bottom side. (d) PSM scans of pellets at 100 MPa, ramping time of 10 minutes, a sintering time of 15 minutes, and a maximum temperature of 698 K. (e) Is an average of the measured Seebeck coefficients along the y-direction and x-directions of PSM scans for the pellet in (d) given by blue circles and the pellet in Fig. 4f represented by green triangles. The red dashed line is the total average Seebeck for the pellet in (d).

An attempt to press a pellet at 773 K was conducted, but the melting point of the mixture was reached during the temperature ramp, and the reaction was terminated by turning off the heating at the onset of a fast displacement. In spite of this, a pellet was recovered and was analyzed by PSM (Fig. S1, ESI†), where the peak in the Seebeck coefficient is at $270\ \mu V\ K^{-1}$ (red color in the PSM scan). The PXRD data from the top side shows the β-Zn_4Sb_3 with a high degree of preferred orientation. This sample is further analyzed by synchrotron PXRD analysis in the section below.

Extra Zn and Sb

In the previous three paragraphs the overall compositions of the pellets were fixed at Zn : Sb = 1 : 1. From Rietveld refinements of the PXRD data it is clear that not all Sb reacts during the sintering and that Zn migrates in the same direction as the current. The PSM scans cannot be used to determine the composition of the individual phases, therefore, in order to investigate how the Seebeck coefficient is influenced by excess Sb or Zn, two nonstoichiometric pellets with either 2 at% extra Sb or Zn were prepared. Furthermore, a stoichiometric pellet was synthesized with an extra 0.10 mm thick Zn-foil placed at the bottom of the inner cavity of the carbon die to see the effect of the Zn migration. These three pellets were synthesized at 100 MPa, using a ramping time of 10 minutes, a sintering time of 15 minutes and a maximum temperature of 723 K. The corresponding PSM scans are shown in Fig. 6a–c. In the pellet with extra Sb (Fig. 6a), two clear regions are visible in the form of a large orange region and small blue area at the top. A thin dark red layer is observed, between these two main regions. The orange phase is the same phase that was observed in Fig. 4d, but no inhomogeneously embedded impurities are evident in this pellet. In the pellet with extra Zn (Fig. 6b), three regions emerge; a large blue layer at the top (Zn_4Sb_3), a dark red region with a peak at $285\ \mu V\ K^{-1}$, and also the orange phase.

If one assumes that defect ZnSb contains Zn vacancies rather than Sb vacancies as previously described in the literature,[28,43] then the orange phase corresponds to ZnSb and the blue/green inclusions are unreacted Sb. The red to dark red regions then correspond to $Zn_{1-x}Sb$ with varying Zn content. Values of smaller x correlate to a larger Seebeck coefficient, until x gets negative and there is a phase transition to the β-Zn_4Sb_3. This is confirmed by EDX measurements (Fig. S4, ESI†), where two EDX line scans reveal a slight decrease in Zn concentration from the bottom to the top of the pellet. A large jump in Zn concentration is observed when the Zn_4Sb_3 layer is reached.

The pellet synthesized with a Zn foil, makes it possible to follow the migration of Zn ions. The large extent of the blue region on the bottom side of the pellet in Fig. 6c, shows that Zn-ions migrate easily through the sample. In a single crystal study by Mozharivskyj *et al.*, the composition of the α-Zn_4Sb_3

phase was found to be as low as Zn : Sb = 3.15(2) : 3,[44] corresponding to a stoichiometry of Zn : Sb = 1.05 : 1. This is very close to the ideal stoichiometry of ZnSb, and suggests that even a slight departure from the 1 : 1 ratio will lead to formation of the Zn_4Sb_3 phase. The fact that Zn_4Sb_3 forms both with and without extra Zn or Sb, and since ZnSb transforms into Zn_4Sb_3, then the following reaction has to be reversible:

$$Zn_{1-x}Sb + yZn \leftrightarrow Zn_{4-z}Sb_3$$

During the heating the current will force the Zn to migrate through powder. From the bottom of the pellet the large amount of excess Zn makes it possible to form the β-Zn_4Sb_3. On the front of β-Zn_4Sb_3 phase a red region of Zn rich $Zn_{1-x}Sb$ is present. Going further towards the top an orange Sb rich region exist. At the top the same red Zn rich $Zn_{1-x}Sb$ is present because of the migrated Zn. This reasoning can explain the rise in the Seebeck coefficient towards the top in Fig. 6e for the pellet made at 748 K.

Optimal conditions for phase pure ZnSb

Based on the data presented above, the optimal conditions for a single step synthesis of phase pure ZnSb are a pressure of 100 MPa, a ramping time of 10 minutes, a sintering time of 15 minutes and a maximum temperature of 698 K. These conditions produce a pellet with a narrow Seebeck coefficient distribution around 215 μV K^{-1}; corresponding to the orange phase in Fig. 6d, and this pellet is analyzed in details in the section below based on synchrotron PXRD data. From PXRD data collected from the surface (Fig. S5, ESI†), there is still 4 wt% unreacted elemental Sb at the bottom; the main body of the pellet is 95.8(3) wt% ZnSb and 4.25(8) wt% Sb, and at the top side there is 20 wt% Zn_4Sb_3. However the homogeneity of the PSM scan indicates a pure electronic phase. In Fig. 6e, average Seebeck coefficients along the *y*- and *x*-direction of the PSM scan are shown, and in both directions there is only a very small spread around the total average value.

Synchrotron PXRD results

As mentioned in the section on the effect of the maximum temperature, the pellet produced with a pressure of 100 MPa, using a ramping time of 10 minutes, a sintering time of 10 minutes and a maximum temperature of 748 K is almost phase pure ZnSb (99.1(2) wt% ZnSb and 0.89(5) wt% Sb), as determined from Rietveld refinement of synchrotron PXRD data on powder extracted from the main body of the pellet. The small amount of elemental Sb would not be possible to identify from conventional in-house PXRD data. The PSM scan in Fig. 4f shows a narrow distribution of Seebeck coefficients, and the average Seebeck coefficients along the *x*- and *y*-direction in Fig. 6e show only a small increase along the *x*-direction.

Very high resolution synchrotron PXRD data were measured at 100 K on five samples in an attempt to identify structural differences between the different ZnSb phases identified by PSM scans. The results from the Rietveld analysis are presented in Table S2 (ESI†). For all samples ZnSb was refined using anisotropic thermal atomic displacement parameters (ADPs) for Zn and Sb, the partial occupation of the Zn site, and all the lower level refinement parameters. Additional β-Zn_4Sb_3 and Sb phases were also refined where applicable. Even though the temperature is below the phase transition of β-Zn_4Sb_3 to α-Zn_4Sb_3, none of the extra peaks from lower symmetry α-phase were visible.

The five samples were chosen to be (i) the pellet made at low temperature (573 K) having a wide distribution of Seebeck coefficients with a peak in the blue region, (ii) the sample made at 773 K that reached the melting point in the synthesis, having a large fraction of the red phase, (iii) the sample made at 748 K that has a narrow distribution in the dark orange region, (iv) the sample made at 698 K with a narrow distribution in the orange phase, and (v) the sample made at 723 K with 2 at% excess Sb.

An example of the data, the theoretical PXRD pattern for the refined model and the difference curve for sample (iv) can be seen in Fig. 7. Even though the samples represent a span of more than 200 μV K^{-1}, there is no trend in any of the structural parameters of the ZnSb phase. The effect of the different electronic phases is believed to be caused by slight differences in Zn content and therefore differences in charge carrier concentrations. Since none of the samples have been doped with other elements, it must be the change in composition mediated by the different synthesis parameters that causes the difference. Refinement of the zinc site occupancy in the ZnSb phase show no trend regarding the differences in the Seebeck coefficient and the amount of vacancies are believed to be smaller than it is possible to refine, as shown theoretically by Bjerg *et al.*[29]

Five unique electronic phases have been identified in the thermoelectric material ZnSb: a green phase S = 165 μV K^{-1}, an orange S = 215 μV K^{-1}, a dark orange S = 235 μV K^{-1}, a red S = 255 μV K^{-1}, and a dark red S = 285 μV K^{-1}. From synchrotron PXRD there is no structural difference between these new electronic phases. This suggests that electronic homogeneity needs to be evaluated for compounds that have ions with large mobilities,

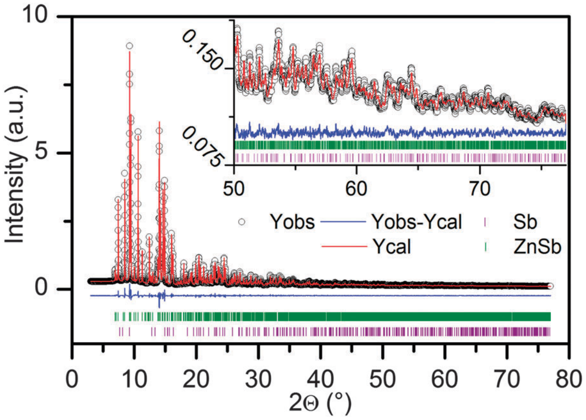

Fig. 7 Rietveld analysis of synchrotron PXRD data measured at 100 K on powder from the main body of the pellet made at 100 MPa, a ramping time of 10 minutes, a sintering time of 15 minutes, and a maximum temperature of 698 K. The model was refined with anisotropic ADPs, free occupancy of Zn, and all the lower level refinement parameters (Table S3, ESI†). The insert shows the high degree of data quality with information in the high 2Θ region and the good agreement of the model to the data.

e.g. $Cu_{2-x}S$, $Cu_{2-x}Se$, Cu_3SbSe_3, $Ag_{2-x}Se$, $Ag_{2-x}S$, $Ag_{2-x}Te$, Zn_4Sb_3, and ZnSb.[18,45–48] Future studies of all the thermoelectric properties for the different phases will hopefully give insight that can aid in understanding the differences.

Multi-temperature synchrotron PXRD analysis

Multi-temperature synchrotron PXRD analysis was conducted, for the sample prepared at an applied pressure of 100 MPa, a ramping time of 10 minutes, a sintering time of 15 minutes, and a maximum temperature of 698 K that has an homogeneous orange phase with S = 215 μV K^{-1}, the sample was cooled to 100 K and heated sequentially to 1000 K. In addition, a data set was recorded when the sample had cooled to 300 K. The data are presented in Fig. 8 along with the Bragg peaks position for the phases at room temperature that are identified in any of the temperatures and Fig. 7 gives an example on a dataset, including the theoretical PXRD pattern for the refined model and the difference curve at 100 K. The refined parameters for the entire temperature series are available in Table S3 (ESI†). The weight fractions as a function of temperature are presented in Fig. 9. This can only be used for studying the stability of the compound in its powder form and not the stability of the pellets. This is because the surface of the powder is much larger than that of the pellet, such oxidation occurs more readily in the powders. However this data still give an indication of the decomposition products.[14] From 100–400 K there is no change in the proportions of the phases, where only ZnSb (95.5 wt%) and Sb (4.5 wt%) are identified. Since the sample was packed under normal atmosphere, already at 500 K ZnO starts to form and the surplus Sb is seen as elemental Sb. Because of the excess oxygen around the heated sample and the relatively low reactivity of Sb compared to Zn, all Zn is eventually converted to ZnO and a minor proportion to the $ZnSb_2O_4$ phase. If this was the same that were to happen for the bulk pellets, ZnSb would be a poor candidate for TE conversion in air.

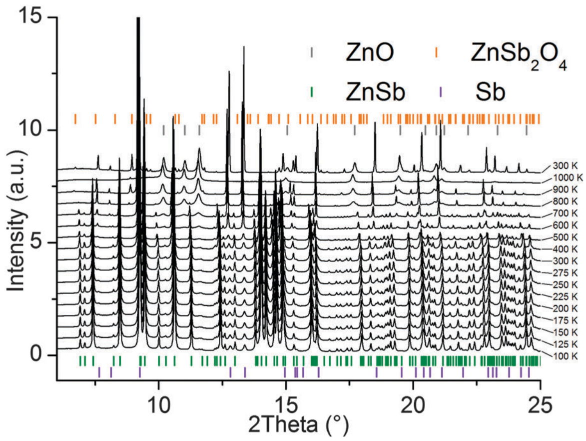

Fig. 8 Multi-temperature synchrotron PXRD data measured on powder from the main body of the pellet synthesized at 100 MPa, a ramping time of 10 minutes, a sintering time of 15 minutes, and a maximum temperature of 698 K.

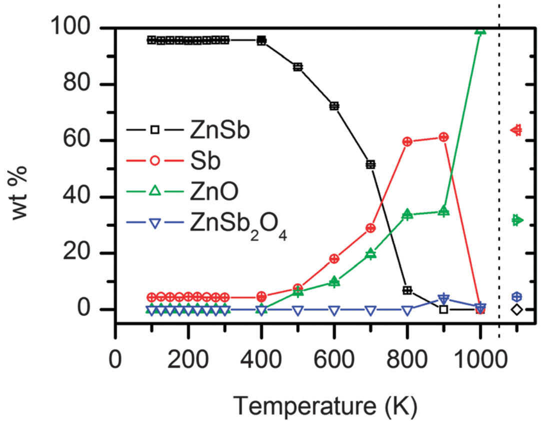

Fig. 9 The weight fractions of the different phases as a function of temperature. This illustrates the stability of floated powder for the pellet made at 100 MPa, a ramping time of 10 minutes, a sintering time of 15 minutes, and a maximum temperature of 698 K with homogeneous orange phase, heated in normal air. The four different phases identified are ZnSb, Sb, ZnO, and $ZnSb_2O_4$. The data point to the right of the dashed line is from the sample at 300 K after cool down.

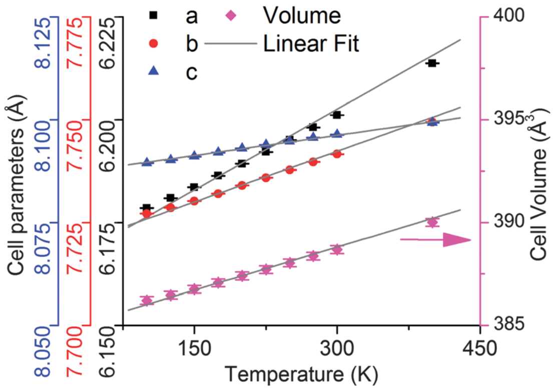

Fig. 10 Cell parameters and volume as function of temperature.

From the multi-temperature PXRD study other useful information can be extracted. In Fig. 10, the cell parameters and the cell volume are plotted as a function of temperature and fitted to a straight line. The slope of the four parts can then be used to find the thermal expansion coefficients *via*:

$$\alpha_i = \frac{1}{a_i}\frac{\partial a_i}{\partial T}$$

where i is one of the three cell parameters or the volume, a_i is the value for i at a given temperature, here 300 K. This gives $\alpha_a = 2.11(3) \times 10^{-5}\ K^{-1}$, $\alpha_b = 1.07(2) \times 10^{-5}\ K^{-1}$, $\alpha_c = 4.05(9) \times 10^{-6}\ K^{-1}$, and $\alpha_V = 3.59(5) \times 10^{-5}\ K^{-1}$. These values correspond very well with recently published values by Fischer *et al.*[49] Proper data for the thermal expansion coefficients have been missing in the literature, and this has been unfavorable for theoretical studies that have calculated significantly larger values than those found experimentally by Fischer *et al.* and in the present study.

The ADPs are in general an estimate of how large the mean square thermal displacement is for one atom. In a single element cubic compound it is possible to model the isotropic thermal motion by assuming a Debye model for the phonons and extract the Debye temperature of the compound:[50]

$$U_{\mathrm{iso}} = \frac{3\hbar^2 T}{m k_{\mathrm{B}} \Theta_{\mathrm{D}}^2}\left[\frac{T}{\Theta_{\mathrm{D}}}\int_0^{\frac{\Theta_{\mathrm{D}}}{T}} \frac{x}{\exp(x)-1}\mathrm{d}x + \frac{\Theta_{\mathrm{D}}}{T}\right] + d^2.$$

where k_{B} is the Boltzmann constant, $\hbar$ is the reduced Planck constant, m is the mass of the atom, d^2 is a disorder parameter,[51] T the absolute temperature and Θ_{D} the Debye temperature. It has become a trend to do this analysis for thermoelectric materials,[52] and even though the theory is not completely correct, useful information can still be obtained, *e.g.*, for inorganic clathrates.[53] It is also possible to use an approximation, and fit the linear part of the data with $U_{\mathrm{iso}} = \frac{3\hbar^2 T}{m k_{\mathrm{B}} \Theta_{\mathrm{D}}^2}$ when $T > \Theta_{\mathrm{D}}$.[50]

In Fig. 11, the ADPs for Zn, Sb and an average of the two as function of temperature are given. Both the full and the linear approximation have been fitted to the ADPs to find the Debye temperatures, Table 1. For the average ADPs an average mass has been used. Since the Debye temperature is the same for both Zn and Sb, the only difference in the development of the thermal motion is because of their mass difference. Neither of the two atoms behave in an abnormal fashion, as is seen for, *e.g.*, the guest atom in the tetradecahedral cage of inorganic clathrates.[53] The values for the ADPs reported by Fischer *et al.* result in the same Debye temperatures, when the correct mass of Sb is used for fitting the full expression, Table 1.[49] Their ADPs are higher which could be due to larger static disorder.[52] In Table 1, data from different theoretical studies are compared. The discrepancy in the Debye temperature determined by the Debye expression and heat capacity measurements, and that from theoretical calculations could be caused by the same disparity in the thermal expansion coefficients. This means that the potentials used for the calculations are slightly incorrect. The fact that the Debye temperatures for the two atoms are so similar may suggests that anharmonic effects are quite similar for the two atoms.

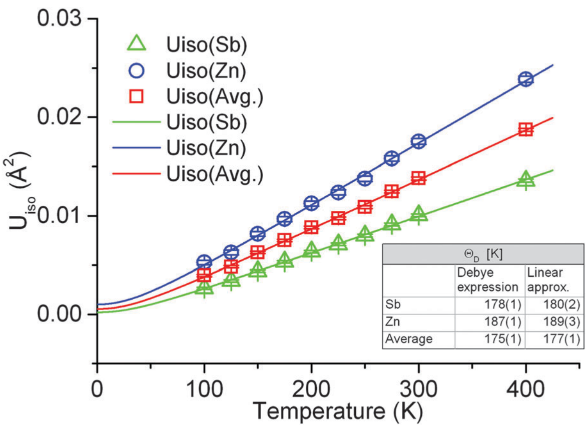

Fig. 11 U_{iso} as function of temperature for Zn, Sb and an average of the two blue circles, green triangles, and red squares, respectively. The solid lines are the fit of the full Debye expression for the ADPs. The table contains the resulting Debye temperatures from the full expression and the linear expression.

Conclusion

SPS has been studied as an efficient method to produce ZnSb pellets in one step for large scale thermoelectric applications. Zn ion migration during synthesis, however, makes it challenging to produce phase pure samples and detailed control of synthesis parameters is required. Multi-temperature synchrotron PXRD data were used to study the thermal expansion, thermal stability and lattice dynamics of the system, and ADPs derived from Rietveld analysis provide an estimated Debye temperature of 175(1) K. The SPS method provides easy access to unknown phases in the Zn–Sb binary phase diagram and it is shown that Zn–Sb is not a line phase. In general, it is questionable whether pellets produced by SPS are homogenous, and thus further processing into modules may suffer from significant variations in the thermoelectric properties, which is a challenge in commercial production as well as in careful scientific studies of the intrinsic thermoelectric properties of the system. On the other hand further optimization of the variation in thermoelectric properties observed throughout the SPS pressed pellets may lead to development of functionally graded materials.

Acknowledgements

This work was supported by the Danish National Research Foundation (Center for Materials Crystallography, DNRF93),

Table 1 Various Debye temperatures for ZnSb

	Fischer *et al.*[49]					Jund *et al.*[43]		Bjerg *et al.*[28]	This study	
				Heat capacity, anharmonic model						
	Debye	Linear Debye	DFT	Single crystal	SPS sample	Heat capacity, calculated	Elastic constants, calculated	DFT	Debye	Linear Debye
Zn Debye [K]	191(1)[a]	197(6)[a]	183	—	—	—	—	—	187(1)	189(3)
Sb Debye [K]	184(1)[a]	190(5)[a]	230	—	—	—	—	—	178(1)	180(2)
Average Debye [K]	180(1)[a]	186(5)[a]	—	195.2	200.5	209.3	236.1	92	175(1)	177(2)

[a] Corrected/recalculated. The original value for the Debye temperature for Sb in the manuscript was calculated with the mass of Zn.

and the Danish Center for Synchrotron and Neutron Research (Danscatt). ABB thanks the SINO Danish Center for funding. The authors would like to thank Dr Hao Yin for fruitful discussions and Dr Hazel Reardon for her help on proof reading the manuscript. We gratefully acknowledge the RIKEN-Harima institute for beam time at BL44B2 at the SPring-8 synchrotron facility.

References

1 T. Caillat, J. P. Fleurial and A. Borshchevsky, *J. Phys. Chem. Solids*, 1997, **58**, 1119–1125.

2 G. J. Snyder, M. Christensen, E. Nishibori, T. Caillat and B. B. Iversen, *Nat. Mater.*, 2004, **3**, 458–463.

3 E. S. Toberer, P. Rauwel, S. Gariel, J. Tafto and G. J. Snyder, *J. Mater. Chem.*, 2010, **20**, 9877–9885.

4 J. Lin, X. Li, G. Qiao, Z. Wang, J. Carrete, Y. Ren, L. Ma, Y. Fei, B. Yang, L. Lei and J. Li, *J. Am. Chem. Soc.*, 2014, **136**, 1497–1504.

5 S. Y. Wang, X. J. Tan, G. J. Tan, X. Y. She, W. Liu, H. Li, H. J. Liu and X. F. Tang, *J. Mater. Chem.*, 2012, **22**, 13977–13985.

6 D. Tang, W. Zhao, J. Yu, P. Wei, H. Zhou, W. Zhu and Q. Zhang, *J. Alloys Compd.*, 2014, **601**, 50–56.

7 J. Nylen, S. Lidin, M. Andersson, B. B. Iversen, H. X. Liu, N. Newman and U. Haussermann, *Chem. Mater.*, 2007, **19**, 834–838.

8 J. Nylen, M. Andersson, S. Lidin and U. Haussermann, *J. Am. Chem. Soc.*, 2004, **126**, 16306–16307.

9 M. C. Record, V. Izard, M. Bulanova and J. C. Tedenac, *Intermetallics*, 2003, **11**, 1189–1194.

10 C. S. Birkel, E. Mugnaioli, T. Gorelik, U. Kolb, M. Panthofer and W. Tremel, *J. Am. Chem. Soc.*, 2010, **132**, 9881–9889.

11 Y. Sun, M. Christensen, S. Johnsen, N. V. Nong, Y. Ma, M. Sillassen, E. Zhang, A. E. C. Palmqvist, J. Bottiger and B. B. Iversen, *Adv. Mater.*, 2012, **24**, 1693–1696.

12 H. Yin, S. Johnsen, K. A. Borup, K. Kato, M. Takata and B. B. Iversen, *Chem. Commun.*, 2013, **49**, 6540–6542.

13 T. Dasgupta, C. Stiewe, A. Sesselmann, H. Yin, B. B. Iversen and E. Mueller, *J. Appl. Phys.*, 2013, **113**, 103708.

14 H. Yin, B. L. Pedersen and B. B. Iversen, *Eur. J. Inorg. Chem.*, 2011, 2733–2737, DOI: 10.1002/ejic.201100130.

15 H. Yin and B. B. Iversen, *Sci. Adv. Mater.*, 2011, **3**, 592–595.

16 B. L. Pedersen, H. Yin, H. Birkedal, M. Nygren and B. B. Iversen, *Chem. Mater.*, 2010, **22**, 2375–2383.

17 B. L. Pedersen and B. B. Iversen, *Appl. Phys. Lett.*, 2008, **92**, 161907.

18 E. Chalfin, H. X. Lu and R. Dieckmann, *Solid State Ionics*, 2007, **178**, 447–456.

19 H. Yin, M. Christensen, N. Lock and B. B. Iversen, *Appl. Phys. Lett.*, 2012, **101**, 043901.

20 T. J. Seebeck, *Ann. Phys.*, 1826, **82**, 133–160.

21 P. J. Shaver and J. Blair, *Phys. Rev.*, 1966, **141**, 649–663.

22 L. T. Zhang, M. Tsutsui, K. Ito and M. Yamaguchi, *J. Alloys Compd.*, 2003, **358**, 252–256.

23 G. J. Snyder and E. S. Toberer, *Nat. Mater.*, 2008, **7**, 105–114.

24 D.-B. Xiong, N. L. Okamoto and H. Inui, *Scr. Mater.*, 2013, **69**, 397–400.

25 D. Benson, O. F. Sankey and U. Häussermann, *Phys. Rev. B: Condens. Matter Mater. Phys.*, 2011, **84**, 125211.

26 U. Haussermann and A. S. Mikhaylushkin, *Dalton Trans.*, 2010, **39**, 1036–1045.

27 L. Bjerg, G. K. H. Madsen and B. B. Iversen, *Chem. Mater.*, 2011, **23**, 3907–3914.

28 L. Bjerg, B. B. Iversen and G. K. H. Madsen, *Phys. Rev. B: Condens. Matter Mater. Phys.*, 2014, **89**, 024304.

29 L. Bjerg, G. K. H. Madsen and B. B. Iversen, *Chem. Mater.*, 2012, **24**, 2111–2116.

30 A. S. Mikhaylushkin, J. Nylen and U. Haussermann, *Chem. – Eur. J.*, 2005, **11**, 4912–4920.

31 X. Song, P. H. M. Böttger, O. B. Karlsen, T. G. Finstad and J. Tafto, *Phys. Scr.*, 2012, **2012**, 014001.

32 C. Okamura, T. Ueda and K. Hasezaki, *Mater. Trans.*, 2010, **51**, 860–862.

33 X. Song, K. Valset, J. S. Graff, A. Thøgersen, A. E. Gunnæs, S. Luxsacumar, O. M. Løvvik, G. J. Snyder and T. G. Finstad, *J. Electron. Mater.*, 2015, 1–7, DOI: 10.1007/s11664-015-3708-6.

34 M. G. Kanatzidis, *Chem. Mater.*, 2010, **22**, 648–659.

35 K. Valset, P. H. M. Böttger, J. Taftø and T. G. Finstad, *J. Appl. Phys.*, 2012, **111**, 023703.

36 M. I. Fedorov, L. V. Prokof'eva, D. A. Pshenay-Severin, A. A. Shabaldin and P. P. Konstantinov, *J. Electron. Mater.*, 2014, 1–6, DOI: 10.1007/s11664-014-3053-1.

37 G. Chen, in *Recent Trends in Thermoelectric Materials Research III*, ed. T. M. Tritt, 2001, vol. 71, pp. 203–259.

38 A. Wrona, K. Bilewska, J. Mazur, M. Lis and M. Staszewski, *J. Alloys Compd.*, 2014, **616**, 350–355.

39 H. Yin, A. B. Blichfeld, M. Christensen and B. B. Iversen, *ACS Appl. Mater. Interfaces*, 2014, **6**, 10542–10548.

40 D. Platzek, G. Karpinski, C. Stiewe, P. Ziolkowski, C. Drasar and E. Mueller, *Proceedings of the 24th International Conference on Thermoelectrics*, 2005, **48**, 13–16.

41 J. Rodríguez-Carvajal, *Phys. B*, 1993, **192**, 55–69.

42 Y. Mozharivskyj, A. O. Pecharsky, S. Bud'ko and G. J. Miller, *Chem. Mater.*, 2004, **16**, 1580–1589.

43 P. Jund, R. Viennois, X. Tao, K. Niedziolka and J.-C. Tédenac, *Phys. Rev. B: Condens. Matter Mater. Phys.*, 2012, **85**, 224105.

44 Y. Mozharivskyj, A. O. Pecharsky, S. Bud'ko and G. J. Miller, *Chem. Mater.*, 2004, **16**, 1580–1589.

45 H. Liu, X. Shi, F. Xu, L. Zhang, W. Zhang, L. Chen, Q. Li, C. Uher, T. Day and G. J. Snyder, *Nat. Mater.*, 2012, **11**, 422–425.

46 K. Funke, *Sci. Technol. Adv. Mater.*, 2013, **14**, 043502.

47 J. B. Wagner and C. Wagner, *J. Chem. Phys.*, 1957, **26**, 1602–1606.

48 M. Kirkham, P. Majsztrik, E. Skoug, D. Morelli, H. Wang, W. D. Porter, E. A. Payzant and E. Lara-Curzio, *J. Mater. Res.*, 2011, **26**, 2001–2005.

49 A. Fischer, E. W. Scheidt, W. Scherer, D. E. Benson, Y. Wu, D. Eklöf and U. Häussermann, *Phys. Rev. B: Condens. Matter Mater. Phys.*, 2015, **91**, 224309.

50 B. T. M. Willis and A. W. Pryor, *Thermal vibrations in crystallography*, Cambridge University Press, Cambridge, 1975.

51 A. Bentien, E. Nishibori, S. Paschen and B. Iversen, *Phys. Rev. B: Condens. Matter Mater. Phys.*, 2005, **71**, 144107.

52 B. C. Sales, B. C. Chakoumakos, D. Mandrus and J. W. Sharp, *J. Solid State Chem.*, 1999, **146**, 528–532.

53 M. Christensen and B. B. Iversen, *Chem. Mater.*, 2007, **19**, 4896–4905.